Performance Evaluation and Characterization of Lithium-Ion Cells under Simulated PHEVs Drive Cycles

by

Pavan Pramod Badami

A Thesis Presented in Partial Fulfillment
of the Requirements for the Degree
Master of Science

Approved June 2016 by the
Graduate Supervisory Committee:

Arunachala Mada Kannan, Co-Chair
Huei-Ping Huang, Co-Chair
Yi Ren

ARIZONA STATE UNIVERSITY

August 2016

ABSTRACT

Increasing demand for reducing the stress on fossil fuels has motivated automotive industries to shift towards sustainable modes of transport through electric and hybrid electric vehicles. Most fuel efficient cars of year 2016 are hybrid vehicles as reported by environmental protection agency. Hybrid vehicles operate with internal combustion engine and electric motors powered by batteries, and can significantly improve fuel economy due to downsizing of the engine. Whereas, Plug-in hybrids (PHEVs) have an additional feature compared to hybrid vehicles i.e. recharging batteries through external power outlets. Among hybrid powertrains, lithium-ion batteries have emerged as a major electrochemical storage source for propulsion of vehicles.

In PHEVs, batteries operate under charge sustaining and charge depleting mode based on torque requirement and state of charge. In the current article, 26650 lithium-ion cells were cycled extensively at 25 and 50 ^{o}C under charge sustaining mode to monitor capacity and cell impedance values followed by analyzing the Lithium iron phosphate ($LiFePO_4$) cathode material by X-ray diffraction analysis (XRD). High frequency resistance measured by electrochemical impedance spectroscopy was found to increase significantly under high temperature cycling, leading to power fading. No phase change in $LiFePO_4$ cathode material is observed after 330 cycles at elevated temperature under charge sustaining mode from the XRD analysis. However, there was significant change in crystallite size of the cathode active material after charge/discharge cycling with charge sustaining mode. Additionally, 18650 lithium-ion cells were tested under charge depleting mode to monitor capacity values.

ACKNOWLEDGMENTS

I would like to express my sincere thanks to Professor A.M. Kannan for giving me an opportunity to pursue master's thesis in his lab and patiently guiding me throughout the research. I would like to thank him for helping me publish research articles in peer reviewed journals during the period of association with him. Secondly, I would like to thank Professor H.P. Huang and Professor Y. Ren for kindly agreeing to be part of my thesis committee and keeping track of progress during research.

I would like to acknowledge Dr. Ravi Mahajan (Sr. Principal Engineer, Intel Corporation) for mentoring me throughout my master's program and giving valuable feedback during my master's thesis. I also want to thank Professor Abdel Ra'ouf Mayyas for providing insight on hybrid powertrains and current profile for research.

Most importantly, I would like to thank my parents for their unconditional support and strength which helped me overcome difficulties during my education. I also want to thank my former advisor and teacher Dr. K. N. Seetharamu (former Professor, IIT madras) who inculcated research culture in me during my undergraduate program, which helped me in carrying out research at Arizona State University.

Lastly, I would like to thank all my friends and lab members for helping me during the thesis through valuable discussions. Special thanks to Liang Shen for helping me in experiments and Rutvik Vaidya for reviewing the thesis. I would like to acknowledge financial support from Salt River Project, AZ during the year 2015-2016.

TABLE OF CONTENTS

CHAPTER Page

LIST OF TABLES

Table Page

LIST OF FIGURES

NOMENCLATURE

LIBs: Lithium-ion batteries.

EVs: Electric vehicles.

PHEVs: Plug-in electric vehicles.

HEVs: Hybrid electric vehicles.

ICE: Internal combustion engine.

Ni-Cd: Nickel cadmium.

Ni-MH: Nickel metal hydride.

LTO: Lithium titanate ($Li_4Ti_5O_{12}$).

LCO: Lithium cobalt oxide ($LiCoO_2$).

LMO: Lithium manganese oxide ($LiMn_2O_4$).

LFP: Lithium iron phosphate ($LiFePO_4$).

$LiPF_6$: Lithium hexafluorophosphate.

FUDS: Federal urban driving schedule.

UDDS: Urban dynamometer driving schedule.

SOC: State of charge.

CS: Charge sustaining.

CD: Charge depleting.

HFR: High frequency resistance.

PC: Propylene carbonate

TEM: Transmission electron microscopy

XRD: X-ray diffraction.

FWHM: Full width at half maximum.

1. BACKGROUND

Automotive industries are currently shifting towards cleaner and sustainable modes of transport in recent years by hybridization of powertrains. As per the EPA reports [1,2], ground transportation accounts for the second largest emission of CO_2, followed by the electricity generated through fossil fuels in the United States. Hence, PHEVs/ EVs are being advocated to significantly reduce greenhouse emissions, as battery technology has great prospects and potential to reduce the demand on fossil fuels. Major challenges lie in reducing the cost of battery systems and increasing their performance [3,4].

LIBs are gaining popularity among hybrid powertrains/all electric drives, due to high energy and power density, and low self-discharge rate compared to Ni-MH and Pb-acid systems [5]. Performance of LIBs depends on electrode materials and most commonly used anode materials in LIBs are C and LTO as they have better reducing properties for lithium. LCO cathode have better rate capability and lower capacity fading, but are not viable for automotive application due to higher costs. Therefore, LFP is the most commonly used cathode material in batteries for automotive applications, due to safety and low cost [6,7].

2. INTRODUCTION TO HYBRID ELECTRIC VEHICELS.

The various types of hybrid vehicles available in the market are micro hybrid, mild hybrid, hybrid, plug-in hybrid (PHEVs) and all electric vehicles. Among these hybrid vehicles, PHEVs and EVs can significantly replace gasoline by operating larger trips by all electric and blended modes. Performance of hybrid powertrains is mainly dependent on the cycle life and power fading characteristics of the battery.

Hybrid electric vehicles consist of two power sources i.e. batteries and ICEs to propel the vehicle. ICEs convert energy from hydrocarbons to mechanical energy by combustion, while batteries operate by converting the chemical energy stored in them to mechanical energy through electric motors.

In HEVs, high peak power demand and quick acceleration is met through electric motor. They also have smaller sized ICEs helping in reduction of CO_2 emissions and improvement in fuel economy [8]. Another feature of HEVs is their regenerative braking system, where energy lost during braking (heat) is recaptured through a generator and fed back to the batteries to charge them while driving.

The PHEVs could be series and parallel powertrain with parallel architecture showing higher efficiencies as detailed in the literature [9,10]. Figure 1 shows schematic of series and parallel powertrains. The series configuration consists of generator and motor and the traction is only provided through motor. Motor receives power either through battery pack or generator operated by ICE [11,12]. Main advantages of series architecture are operation of ICE is in the optimum region of efficiency and a single torque source, which simplifies speed control. Series configuration is generally used in heavy duty vehicles due to simplicity of its architecture, speed control, and packing, but the major disadvantage is high loss of energy during conversion due to a large number of mechanical parts.

In the case of parallel architecture, traction is provided by ICE or battery pack in tandem arrangement, while batteries are recharged through motor/generator during coasting and braking. The major advantages of parallel architecture are low energy losses due to less mechanical parts, and compactness, making it viable for passenger vehicles.

The disadvantages here are the complex structure of parallel powertrains and that the ICE operating points cannot be fixed in the optimum region of operation [8].

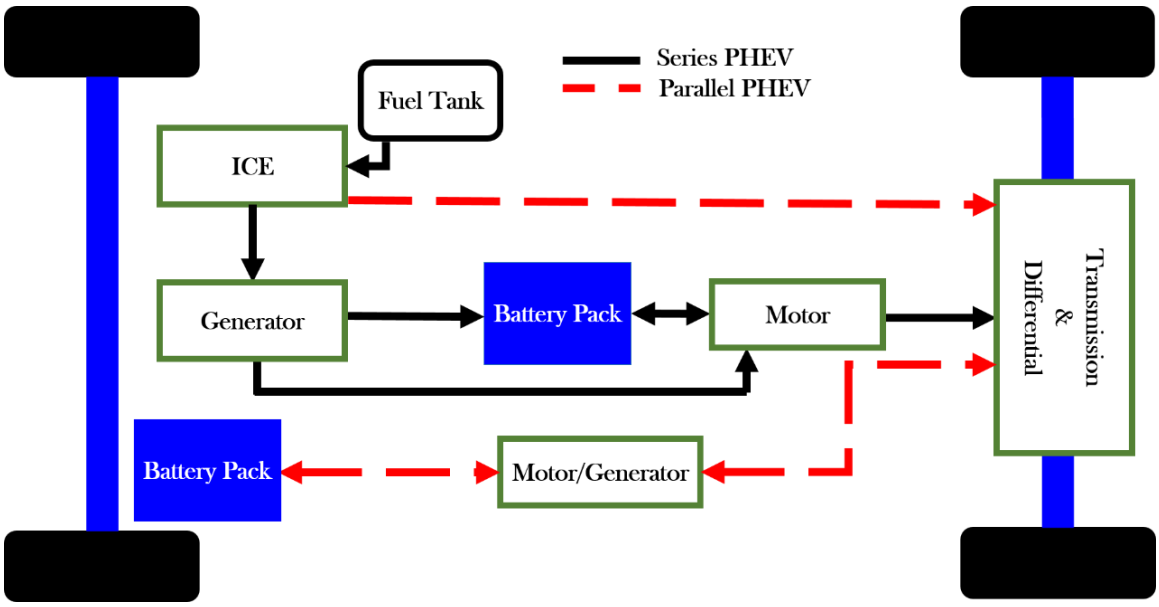

Figure 1. Schematic of series and hybrid powertrain.

3. LITHIUM-ION BATTERIES

3.1 Battery Chemistry Overview

Batteries are the most economical electrochemical system to store energy. It consists of anode (negative electrode), cathode (positive electrode) and a porous membrane separator. Performance of batteries is generally determined by specific power density (W/kg), specific energy density (Wh/kg), voltage characteristic, life cycle and temperature operating window. Lead acid batteries are most economical due to low cost of raw materials but are not suitable for hybrid powertrains due to their low energy and power density. However, lead acid batteries are more suitable of micro and mild hybrids due to

their inherent safety, ruggedness and high recycling values. On the other hand, Nickel-cadmium battery shows better energy and power density. Cadmium being a toxic material, disposal is one of the biggest issues. Nickel metal hydride (Ni-MH) batteries are advanced version of Ni-Cd batteries, carrying much high energy and power density without any toxic materials harming the environment. Ni-MH batteries consist of nickel hydroxide as cathode and metal hydride consisting of an alloy of vanadium, titanium, nickel and other metals. Ni-MH batteries are most popular among HEV powertrains due to safer operations at high voltage, high gravimetric energy and power density, tolerance to overcharge and discharge and a larger temperature operating window [13,14].

Sodium-nickel chloride batteries suffer from low power capabilities although they have higher energy densities. These batteries have lower temperature operating window and high resistances. LIBs are advantageous compared to other systems due to high power and energy density, low self-discharge and larger temperature operating window, making them lucrative for automotive applications. Figure 2 shows Ragone plot for various battery systems comparing their specific energy (Wh/kg) with specific power (W/kg).

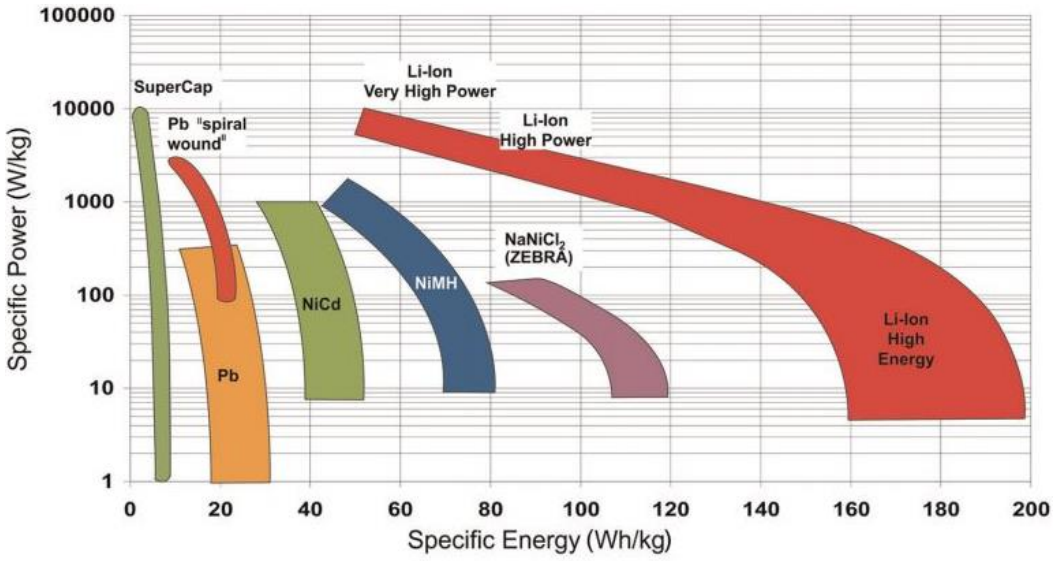

Figure 2. Ranoge plots for various battery chemistries [14].

3.1.1 Types of Lithium-Ion Batteries

Primary LIBs were commercially available in 1970s for military applications. Lithium being light weight with high electrochemical equivalence and good ionic conductivity, makes it is an attractive anode material [15]. LIBs also show flatter discharge voltage characteristics. Secondary LIBs are rechargeable consisting of Li^+ host material which helps in shuttling Li-ions from anode to cathode and vice versa, depending on charging or discharging of the battery. Secondary LIBs consist of anode, cathode and electrolyte as seen in Figure 3.

Generally, anode materials are classified on type of reactions like intercalation, conversion and alloying. Most widely used anode materials for intercalation are graphite and LTO. Intercalation is incorporation of Li^+ ions into the structure of electrode materials. However, LTO is highly reversible but has lower capacity and voltage compared to graphite [16]. Most commonly used cathode materials are LCO, LMO, and LFP and the battery

characteristics change with cathode materials. The radar chart (Figure. 3) summarizes performance of LIBs for different cathode and anode materials based on specific energy, specific power, thermal stability, discharge voltage and life time. Among all the LIB chemistries, LFP provide excellent safety and thermal stability compared to other chemistries with relatively less cost/cycle excluding LTO/LCO.

Electrolyte acts as a medium for ion transport between electrodes during charge and discharge completing the circuit. Electrolytes are electrically resistant to prevent short circuiting of batteries. Separators behave as barriers to prevent physical contact of the electrodes, but allows ions transfer through it. LIBs can incorporate four different kind of electrolytes namely liquid solution of lithium salts, polymer, ceramic and gel based electrolytes, along with $LiPF_6$ salts. Liquid solution based electrolytes are most commonly used in LIBs for PHEV applications [17].

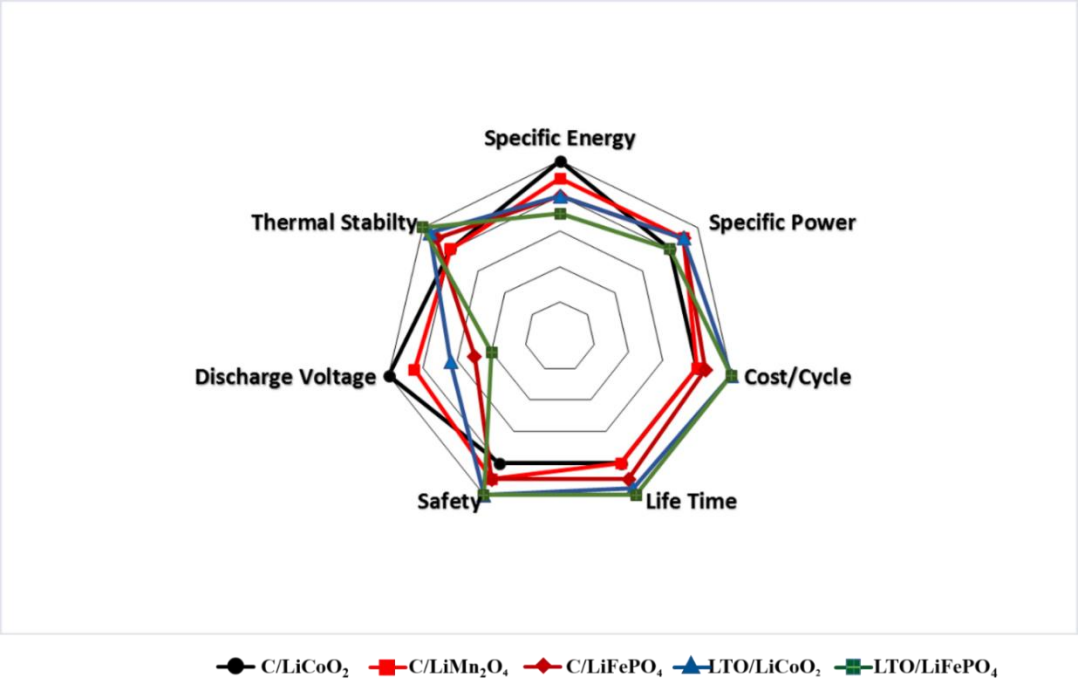

Figure 3.Performance comparison of different LIB chemistries.

During discharge, Li^+ ions travels from anode to cathode releasing electrons to external circuit oxidizing the anode given by Eq. (1), while charging, Li^+ ions travel from cathode to anode and electrons are transferred from the external circuit to reduce the cathode as given by Eq. (2).

Discharge

$$Li_xC \longrightarrow Li^+_{x-0.5}C + 0.5e^- + 0.5Li^+ \quad (1)$$

Charge

$$Li_{0.5}FePO_4 + 0.5Li + 0.5e \longrightarrow LiFePO \quad (2)$$

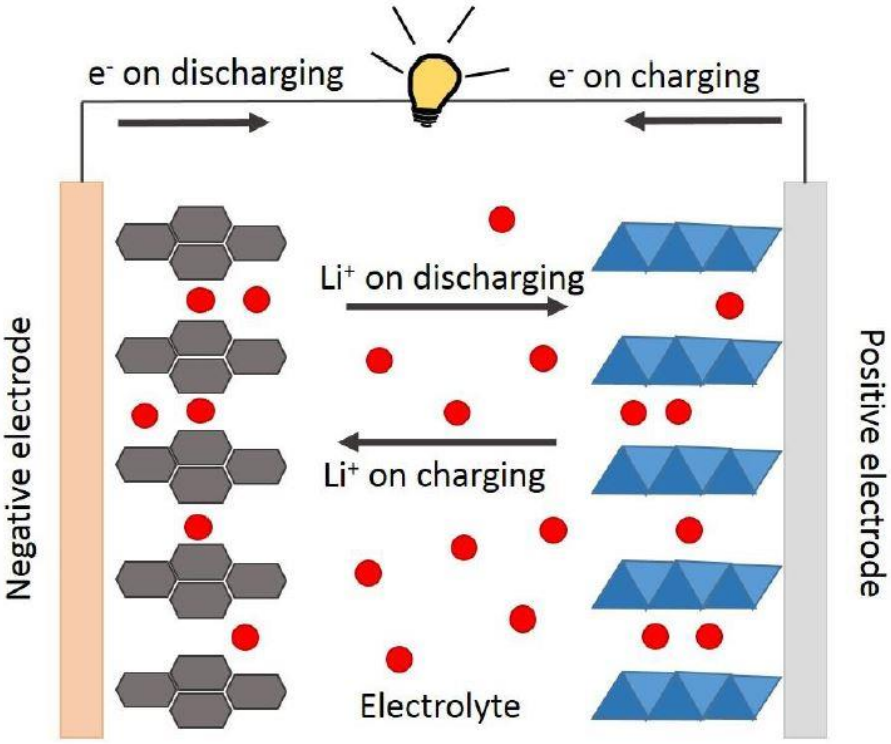

Figure 4 Lithium-ion Battery operation [18]

4. LITERATURE REVIEW

In recent years, LIBs have gained interest among electronic devices and automobile applications due to high gravimetric, volumetric, energy and power densities with low self-discharge rates as compared to other batteries [19]. The LFP is as an excellent cathode material with a flat discharge voltage of 3.5 V vs Li [20]. As LFP is not highly conducting (electronic conductivity: 10−9 S cm−1), the rate capability is being improved by carbon coating [21,22]. Han *et al.* [23] reported the capacity fading for commercial LIBs with NCM/LTO, LFP/C and LMO/C under EV loads using hybrid pulse power characterization. Among various systems evaluated, the LFP cathode material showed the best capacity retention with more than 1000 cycles before end of life. Based on this data, a life cycle

model based on genetic algorithm was also developed and was in good agreement with < 1% error.

Ramadass *et al.* [24] studied capacity fading of Sony cylindrical 18650 Li-ion (LCO cathode) cells at various temperatures using CC-CV protocol. The higher capacity fade at elevated temperatures was ascertained due to SEI layer formation at the surface of the anode, resulting in cell impedance rise and lithium loss. In addition, Ramadass *et al.* [25] also reported three major reasons for capacity fading, (a) loss of secondary active material (LCO/C), (b) primary active material (Li^+) and (c) rate capability loss. It was observed from the XRD analysis of the cycled cathodes that the *c/a* ratio decreased with cycling and temperature, leading to decreased Li stoichiometry.

Zhang *et al*. [26] reported capacity and power fading of prismatic Li-ion (LFP cathode) cells at various temperatures under constant charge/discharge protocol and FUDS with EV mode. For the first 300 cycles, batteries were cycled at 3C rate (charge/discharge), later EV current profile was implemented for the next 300 cycles under the operating window of 80-30% SOC. They concluded capacity and power fade is severe at lower temperatures (-10 and 0 ^oC) thus making LIBs with LFP cathode unsuitable for low temperature operations.

Capasso *et al*. [27] evaluated $Li[NiCoMn]O_2$ (LNCM) and LFP battery packs using CC-CV protocol and dynamic current using trapezoidal wave form. The LIBs with LFP cathodes showed no significant capacity fading with both stationary and dynamic operating conditions compared to that with LNCM.

5. OBJECTIVE

The primary objective of the research is to understand the performance of commercial 26650 LFP cells subjected to charge sustaining mode under FUDS drive profile at room temperature and elevated temperature. The article provides detailed insight on capacity fading, impedance and characterization of 26650 cells under both modes at 25 ^{o}C and 50 ^{o}C. Additionally, 18650 $LiFePO_4$ cells are tested to charge depleting mode under FUDS driving profile for future study. Practically, in PHEVs/EVs battery packs temperature reaches above 45 ^{o}C with active thermal management systems [28]. In past and recent, there have been cases reported on poor performance of batteries and EVs setting to flames due to battery failures at high temperatures. Batteries of Nissan LEAF (EV) showed extensive capacity fade in hotter climatic regions like Arizona, Texas and California, forcing the company to shift toward new chemistries [29]. Therefore, it is very critical to understand failure mode/ cycle life of batteries for hot and dry weather.

6. EXPERIMENTAL

6.1 Battery Structures

LIBs are generally packed in the form prismatic, cylindrical, coin and pouch structures as detailed in Figure.5. Most commonly used battery structure in EVs and PHEVs are cylindrical and prismatic form, due to large surface of cathodes and lesser weight. These batteries are built by winding electrodes and separators immersed in electrolyte. Cylindrical lithium ion batteries are classified based on their physical dimension of cylindrical case, for example 26650 cells has 26 mm diameter and 65 mm length.

Figure.6 shows cross-section view cylindrical batteries. Cylindrical batteries consist of anode and cathode separated by microporous separator made of polyethylene or polypropylene. Cathodes consist of aluminum foil coated with active material on both side and anode is made of copper foil coated with graphite/carbon active materials. Aluminum and copper acts as current collectors during charge and discharge [15].

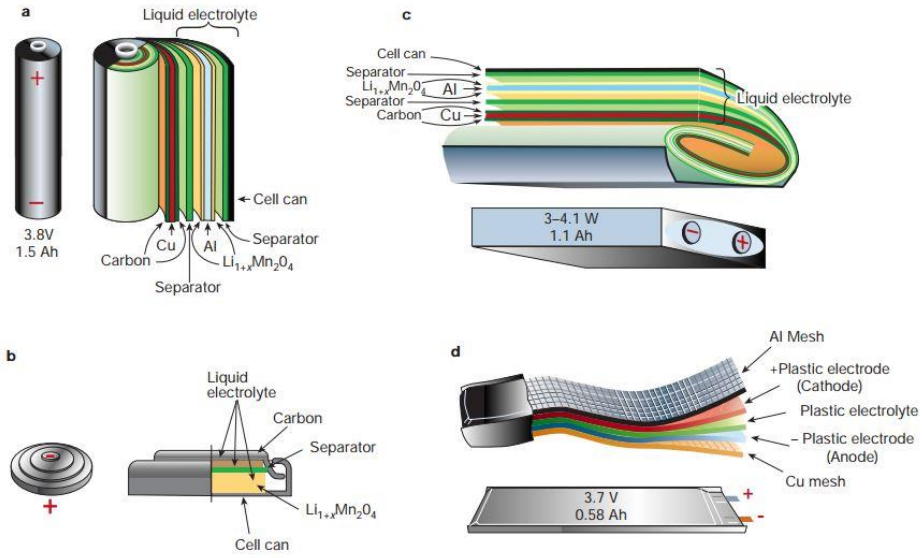

Figure 5.Various battery configurations [30].

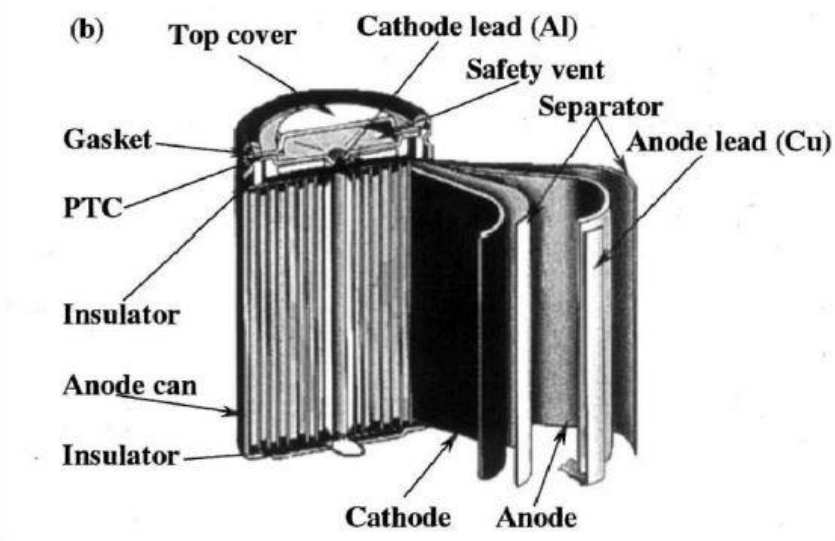

Figure 6.Cross-sectional view of cylindrical LIB battery [15].

6.2 PHEVs Driving Profile.

In our present work, batteries are subjected to typical FUDS driving patterns published by EPA [31] for light duty vehicles as in Figure.7. FUDS represent driving pattern inside city for light duty vehicles, which includes frequent stop, sudden acceleration and braking. Time length of duty cycle is 1369 s with average speed of 19.59 mph and covering distance of 7.45 miles. Maximum speed during FUDS drive cycle is 55 mph, and drive cycle starts with cold start. PHEVs are beneficial for urban driving due to their higher electric range compared to HEVs, thereby reducing dependency on ICEs to propel the vehicles. Therefore, it is essential to understand battery performance of batteries based on FUDS behavior.

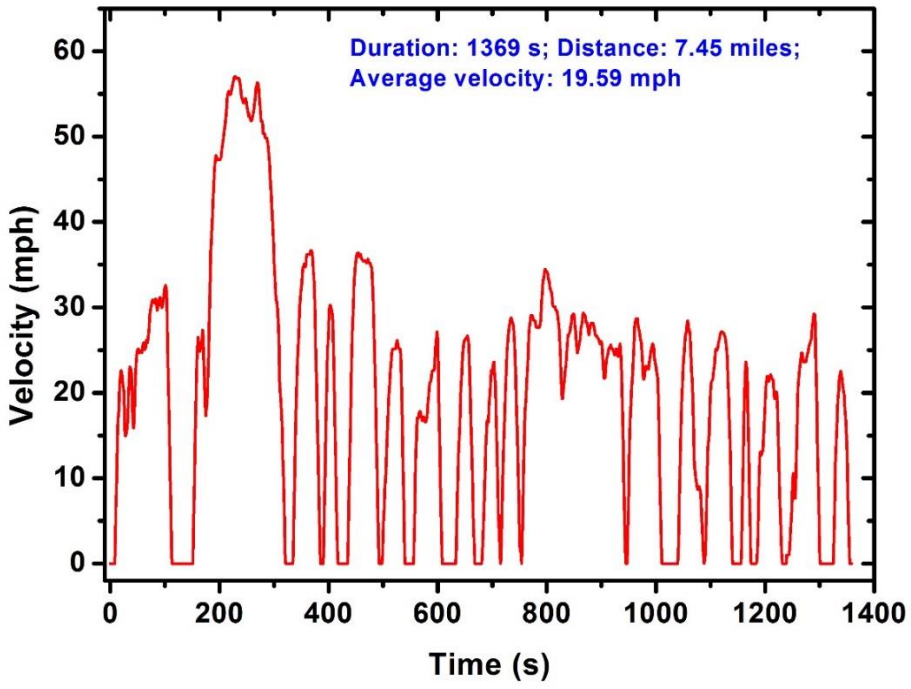

Figure 7. FUDS drive cycle

6.3 Energy Management Strategies

Energy management strategies/ supervisory control determines power split between the ICE and batteries during propulsion of vehicles, which essentially determines fuel economy and emissions in hybrid vehicles. There are many control strategies as detailed in [32], among them ECMS shows highest fuel economy. Equivalent consumption minimization strategy (ECMS) developed by Paganelli *et al*. [33,34] minimizes fuel consumption locally at instantaneous time, reducing global optimization time given by Eq. (3), where $\dot{m}_f(t)$the actual fuel consumption by ICE and $\dot{m}_{fem}(t)$ is equivalent fuel consumption by electric motor. Total power required to propel the vehicle is split between ICE and battery as shown in Eq. (4).

$$\dot{m}_{feq}(t) = \dot{m}_f(t) + \dot{m}_{fem}(t) \quad (3)$$

$$P(t) = P_{ICE}(t) + P_{Battery}(t) \quad (4)$$

Figure. 8 shows the current profile during electric motor assist for FUDS driving schedule based on ECMS retrieved from Kumar *et al*. [35,36] Simulink model. This model is built considering parallel through the road hybrid electric vehicle (PTTR-HEV) for a cross over SUV Chevrolet Equinox and Table 1 describes vehicle dynamics parameters. Total traction force required to propel the vehicle is given by Eq. (5).

Input for the ECMS model is the velocity profile supplied to the driver block, while PID algorithm determines torque requirement based on it. Supervisory control splits the torque between ICE and battery based on the ECMS algorithm depending on the dynamics of the vehicle and torque-speed efficiency map of the ICE and electric motor [36]. Model also accounts for regenerative braking to charge the battery. Torque required to set the vehicle in motion is given by Eq. (6) where R is radius of tires and the current (I) drawn from battery pack is proportional to torque (T) at wheels given by Eq. (7).

$$F_{total} = ma + \frac{1}{2} C_d \rho A_f v^2 + mgc_{rr} \quad (5)$$

$$T = F_{total} * R \quad (6)$$

$$T \propto I \quad (7)$$

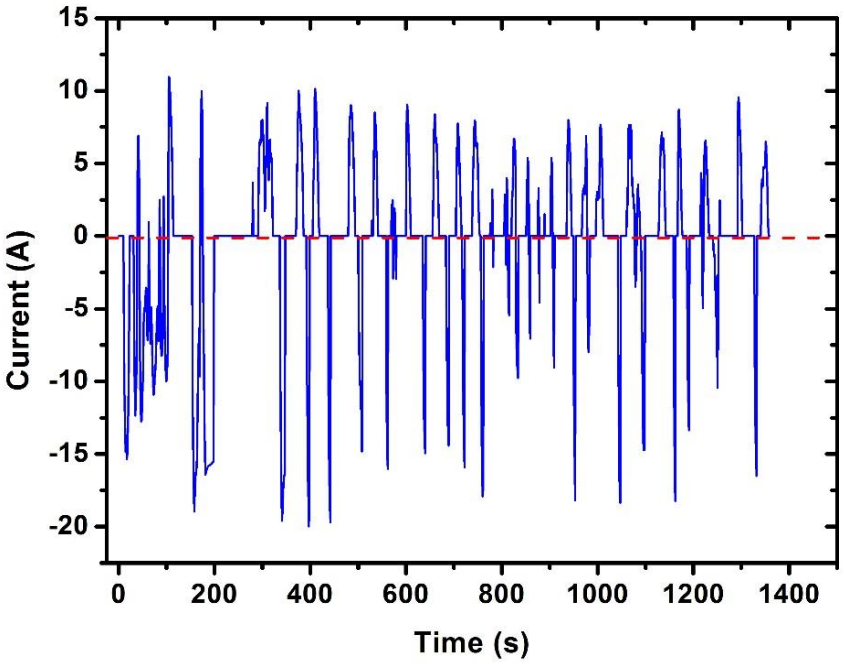

Figure 8. Current profile charge sustaining mode

Table 1. Vehicle dynamic parameter

Parameter	**Value**
Tire Radius, R	0.3305 m
Vehicle Mass m	2000 kg
Gravitational Acceleration, g	9.8 m/s^2
Air Density, ρ	1.29 kg/m^3
Frontal Area, A_f	2.82 m^2
Aerodynamic Drag Coefficient, C_d	0.416
Road grade	$\propto$ rad
Coefficient of rolling resistance	C_{rr}

Figure. 9 represent current profile under charge depleting mode. Current profiles for CD mode were derived based on acceleration and deceleration given by Eq. (8) and (9).

$$I_{discharge} = \frac{dv}{dt} \quad (8)$$

$$I_{charge} = (-\frac{dv}{dt}) * 0.07 \quad (9)$$

$$F_{total} = m * a, \text{ where } (a = \frac{dv}{dt}) \quad (10)$$

Under CD mode, force due to rolling resistance of the vehicle and drag force is neglected considering an ideal case, while force needed to propel vehicle is given by Eq. (10). Simulated current is highly transient compared to actual current considering rolling resistance and drag force. In order to simulate the effect of charge during regenerative braking, 7% of the total deceleration power is fed as regenerative charge and mass of the vehicle is taken as 1588 kg from Peterson *et al*. [37].

CS current obtained from the model was scaled between +20 to –20 A for experimental testing on 26650 cells, due to current limitation with the battery cycler. While, 18650 cells where subjected to CD current scaled between +30 to –30 A on acquiring new battery cycler. Positive current denotes the charging, while negative denotes discharge.

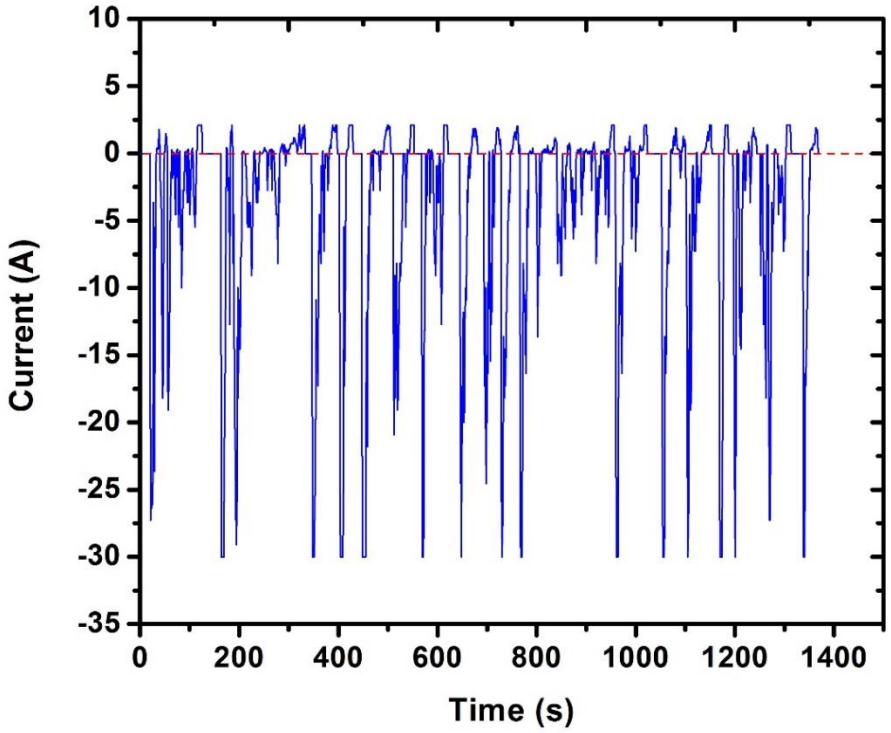

Figure 9. Current profile charge depleting mode.

6.4 Cycling Procedure.

Charge/discharge cycling of cylindrical 26650 Li-ion cells (C/$LiFePO_4$) was carried out using advanced battery cycler Arbin -BT2000 series channels with current range of -20 to 20 A (see Figure. 10). Battery pack with capacity 5 Ah were subjected to PHEV current load under CS mode at room temperature (25^oC) and elevated temperature(50^oC) .To verify capacity rating and columbic efficiency, batteries were initially cycled (5 cycles) at 1C rate with cut off charge and discharge voltage values of 3.6 and 2.0 V respectively and 5 minutes of rest between cycles. A Thermo Electron Corporation thermal chamber was used to maintain the batteries between 49-51 ^oC.

(1) Cells were completely charged at 1C rate until 3.6 V (100 % SOC) using CC-CV charging method; (2) Rest time of 5 minutes was introduced before subjecting batteries to dynamic current load under CS mode using FUDS driving schedule with time length of 1369 s; (3) Cells were charged at 1C rate, and then cycled back under PHEV current (step 2) 5 times in total; (4) Later, cells were discharged at 1C rate until 2.0 V with rest of 10 minutes between charge (step 3) and discharge (step 4); (5) Constant charge at 1C rate (until 3.6 V) with rest time 10 mins was introduced after step 4; (6) Capacity and impedance characterization of batteries was carried out at 100 % SOC of the batteries. Figure. 11 describes flow diagram of the cycling procedure.

Batteries under CS mode require nearly 19 continuous FUDS cycles to deplete from 3.6 to 2.0 V, number of FUDS cycles needed to completely drain the battery from defined as a drive cycle. Five such drive cycles along with a cycle along with a constant charge and discharge cycle at 1C rate is defined as one cycle in our experiment.

Figure 10. Arbin BT-2000 Series

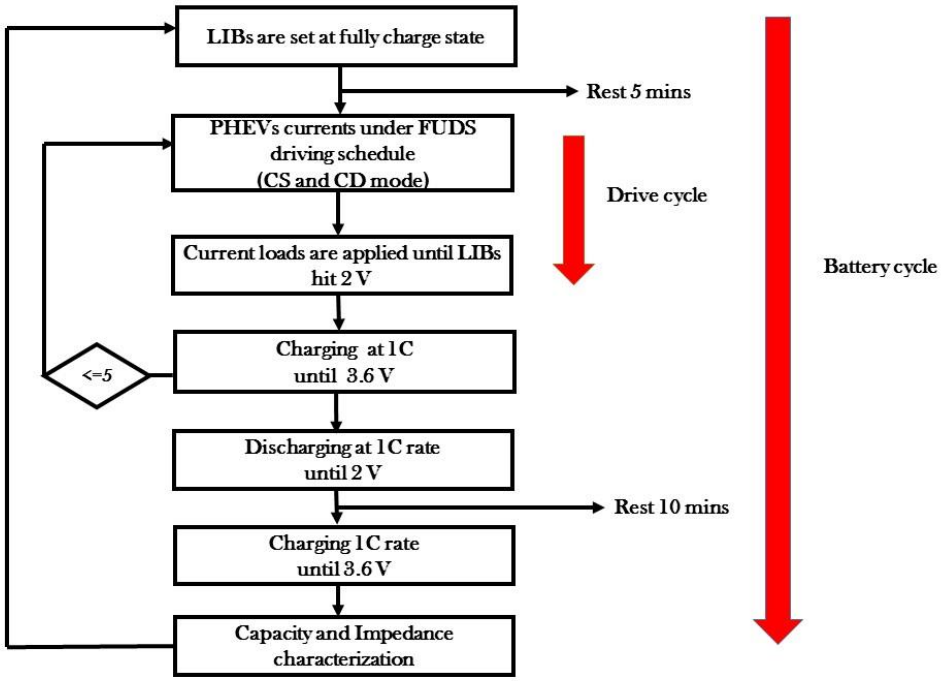

Figure 11. Cycling procedure flow chart.

6.5 EIS and XRD Analysis

6.5.1 Electrochemical Impedance Spectroscopy

Electrochemical impedance characterization is most widely used noninvasive technique to understand cell behavior at different operating temperature and SOC in order to get better insight into electrochemical systems. EIS was carried out with PARSTAT 2273 (Figure. 12) using a single sine wave method [38]. Single sine wave method works on the principle of constant amplitude and pulsed varying frequency inside the battery. Amplitude of the wave was set at 50 mV for the frequency range from 1 KHz to 10 mHz with 30 points per decade frequency, which was determined experimentally. The counter electrode and reference electrode leads of PARSTAT were connected with negative terminal of the cell, while the working electrode and sense electrode leads were connected to the positive terminal of the cell before EIS characterization.

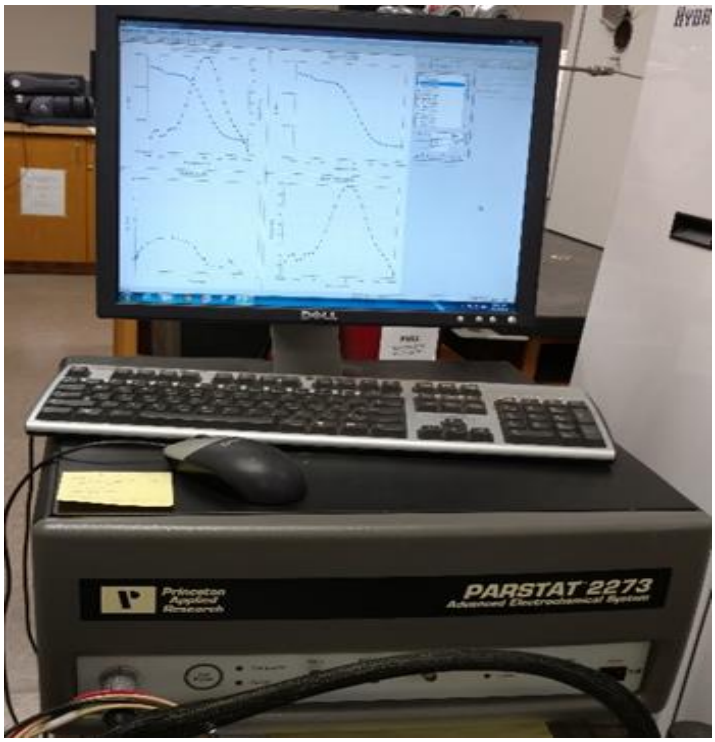

Figure 12. PARSTAT 2273

6.5.2 X-Ray Diffraction Analysis

For XRD analysis of the cathode material, the cycled battery was completely discharged to 0 V using an E-load, and were cut horizontally upon complete discharge. After taking off the canister, cathode material coated on aluminum foils were collected in powdered form using plastic knife on washing with ethanol and distilled water before use, to avoid contamination of the sample.

200 milligrams of each cathode sample collected from uncycled (fresh), CS mode cells, were soaked with 10 ml propylene carbonate (PC) solvent [39], followed by 5 minutes of sonication and 10 minutes of stirring using magnetic stirrer. After stirring, solution was carefully decanted using a syringe to prevent loss of material and above procedure was repeated until a clear solution was obtained. Powered sample on decantation was vacuum

dried overnight at 50 ^{o}C using high temperature vacuum oven. This process is carried out to obtain pure LFP, to get rid of $LiPF_6$ salts present inside electrolyte for XRD analysis.

XRD analysis on powdered cathode electrode was carried out on a Bruker diffractometer using Cu anode (Cu-k_α radiation of 1.54 Å). The patterns were recorded for an angular range (2θ) between 20 and 80 degrees with step size of 0.05 degree per second, and unit cell analysis and peak detection was done using JADE 5.0. Software.

7. RESULTS AND DISCUSSIONS

Figure.13 shows discharge and charge profiles of batteries under CS mode at room temperature (after 6 cycles). In CS mode, batteries take about 7.2 hours to discharge to 2.0 V. Nearly flat voltage plateau is observed during discharge in the middle portion, while a quick voltage drop is observed at the beginning and at the end. Accelerated cycling tests performed on battery under CS modes showed different capacity fading characteristics at room temperature (25 ^{o}C) and elevated temperature (50 ^{o}C).

Figure. 14 shows cyclability data for batteries tested under CS mode at room temperature and elevated temperature. Cells under CS mode underwent 337 cycles, which took nearly about 8 months to complete the cycle number.

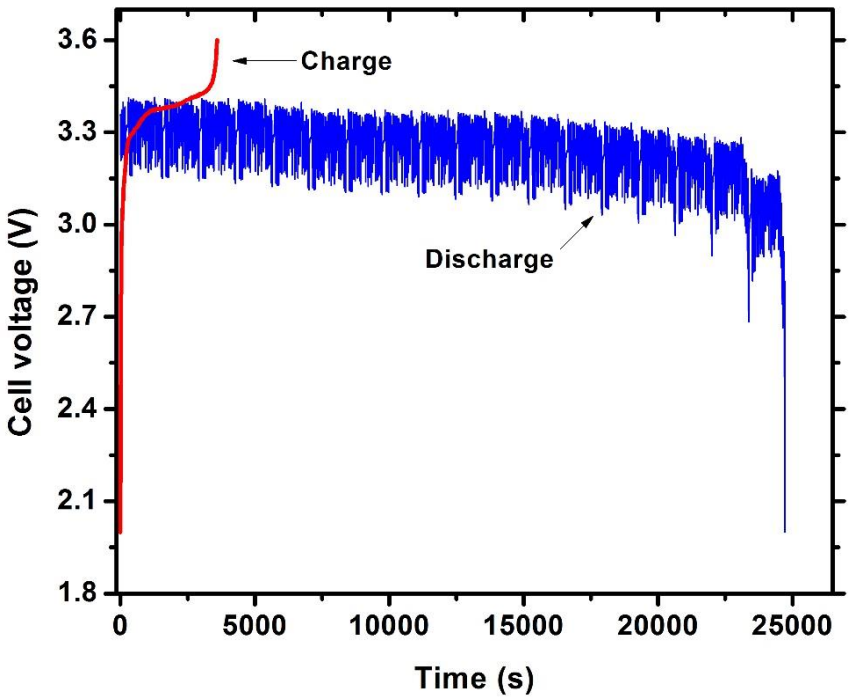

Figure.13 Charge and discharge characteristics under charge sustaining mode

On cycling batteries at room temperature with CS current load, discharge capacity values after the 1st cycle was found to be 4.95 Ah, with columbic efficiency nearly 98 %. Cells were initially cycled at room temperature to understand degradation rate. After 49th cycle, cells showed capacity loss of 1.6%. Later, Cells were subjected to elevated temperature testing as cells at room temperature showed good capacity retention after 49 cycles. Interestingly, at 50 ^{o}C cells showed higher discharge capacity values (5.16 Ah) (after 55th cycle) compared to the discharge capacity values at 25 ^{o}C. Rise in capacity value is mainly attributed to higher electrolyte conductivity. Capacity drop per 200 cycles at high temperature was approximately 3.7% and sharp drop in capacity value was observed at

211th cycle from to 4.822 to 4.806 Ah. (see Figure. 14). Cells cycled at 50 °C after 337 cycles showed capacity loss of 13% under CS current profile.

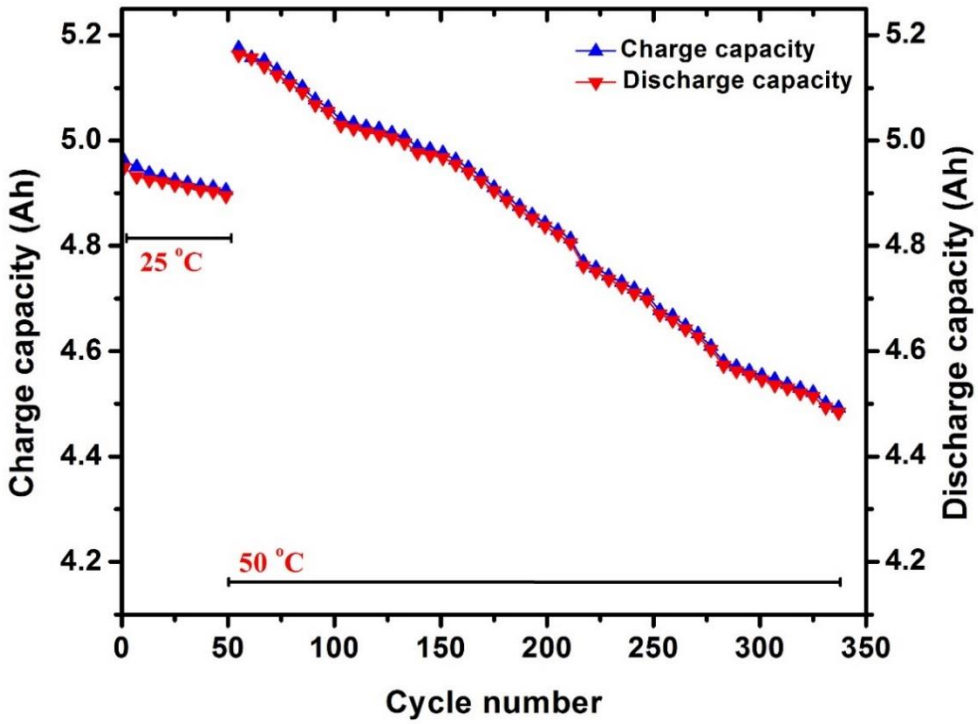

Figure 14. Cyclability data of cells under charge sustaining current

Table 2 Percentage capacity fade of cells under CS mode

Operating conditions	26650 LIB (5.5 Ah)						
Cycle Number	31	49	109	169	229	289	337
25 °C	0.74	1.06	-	-	-	-	-
50 °C	-	-	2.70	4.62	8.27	11.62	13.15

Theoretically impedance spectra of LIBs (see Figure. 15) consist of an inductive tail at high frequency (section 1), ohmic resistance (section 2) which is summation of resistance offered by electrolyte, current collector and separator. Two semicircular arcs at mid frequency are attributed to SEI layer (section 3) and charge transfer resistance at the electrodes (section 4). The tangential line in EIS spectra is due to diffusion process between electrodes at lower frequency (section 5) [40]. However, the measured spectra show deviation from theoretical response, as many processes are still not well understood.

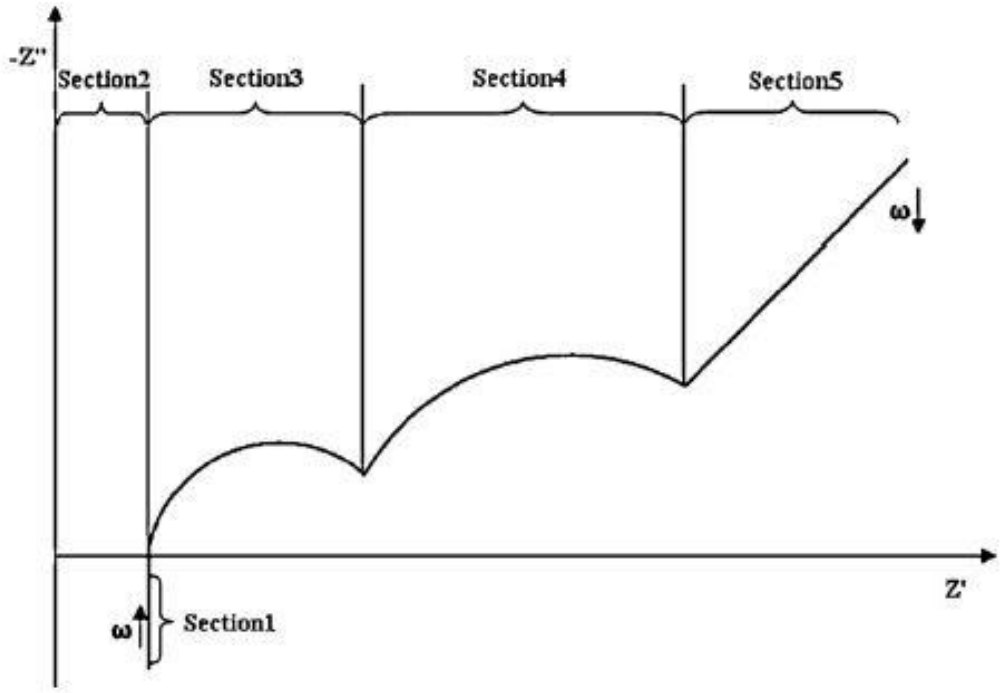

Figure 15. Theoretical Nyquist plot for LIBs.

Figure. 16 show impedance spectra for CS at room temperature for 100 % SOC. It is seen that the impedance spectra show an inductive tail at high frequency, semicircular arc and sloped line at mid and lower frequency for all the cycles at room temperature. The only

notable difference in the spectra with change in cycle number is increase in ohmic resistance of the cells, which is represented by high frequency intercepts on Z_{re} axis. Initial HFR of the batteries prior to subjecting PHEV loads were noted to be nearly 5 mΩ for but after 43 cycles under CS mode impedance rise was found to be 6.3 mΩ . EIS spectra were analyzed using EC-lab to develop equivalent circuit model using (Randomize + simplex technique). The convergence was achieved on 5000 iterations with R^2 value of 0.89. Circuit consists of inductor (L), resistor(R1), capacitor (C), resistor (R2) and Warburg impedance (W) as seen in Figure. 16. With cycling, (R1) and (R2) values were found to increase but no much change in Warburg impedance was observed.

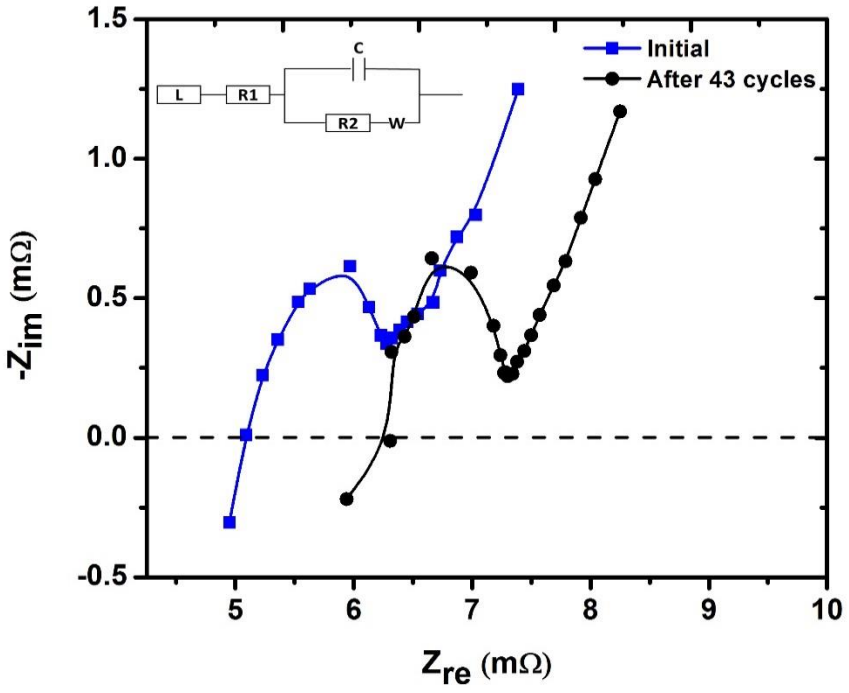

Figure 16. EIS at room temperature under charge sustaining mode

Impedance patterns are highly dependent on temperature and SOC of batteries. Ohmic resistance decreases with increase in temperature, as electrolyte ion conduction increases with temperature. Overall cell resistance increases with cycling at elevated temperatures due to loss of active material and carbon, leading to formation of SEI layer on anode. Another factor could be evaporation of the electrolyte during high temperature cycling.

Figure 17. shows impedance spectra under CS mode at 50 ^{o}C. EIS shows a stronger gradient sloped line due to higher diffusion and a smaller semicircular arc at mid frequencies due to low charge transfer resistance. Ohmic resistance values are found to be much lower (4.61 mΩ) after 55th cycle under CS mode as compared to the 43rd cycle (6.3 mΩ). Impedance value at the end of 337 cycles was found to be 7.5 mΩ under CS mode. Although trends at high temperature were similar to room temperature.

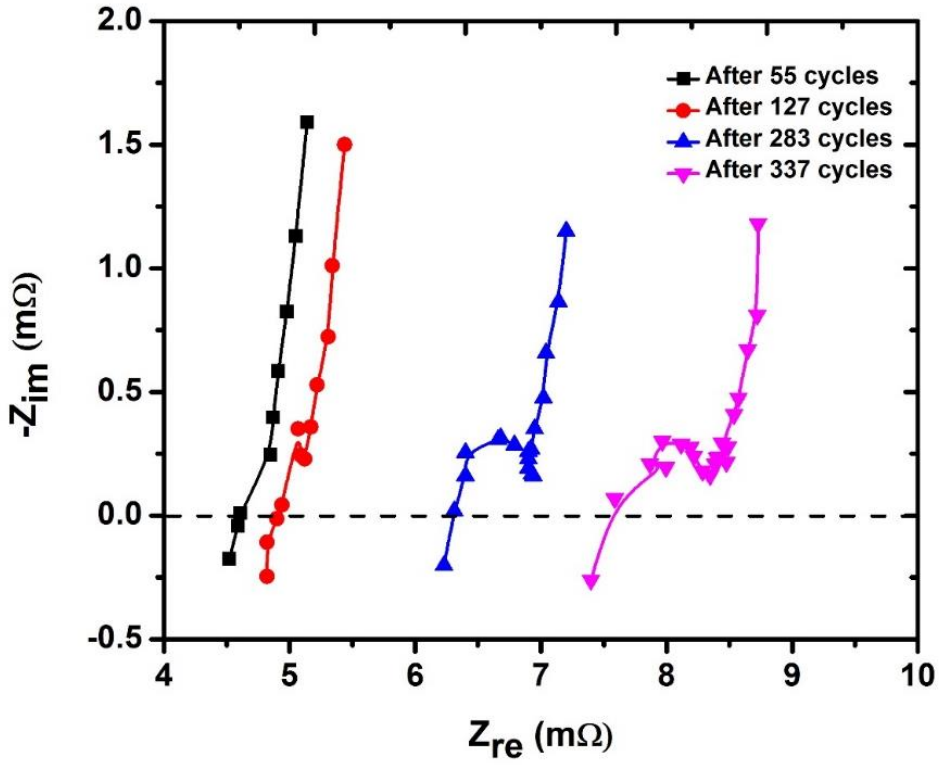

Figure 17.EIS at elevated temperature under charge sustaining mode

Fig.18 shows XRD patterns for uncycled (fresh) and charge sustaining cathode materials perfectly indexed to orthorhombic system of olivine type. Sharp intense peaks were observed for triphylite phase ($LiFePO_4$-*), while no heterosite peaks ($FePO_4$) were detected for fresh and charge sustaining samples. Maximum intensity peak for $LiFePO_4$ was at 2θ = (35.6^o - 35.9^o) for all the two cases. Fully lithiated electrode showed highest peak broadening, while CS mode electrode showed less broadening at highest intensity peak and characteristic $LiFePO_4$ peaks were found to be similar to Padhi *et al*. [20].

Highest $LiFePO_4$ peak intensities for the two electrode materials were found in lattice plane (131), and the corresponding crystallite sizes using FWHM were determined to be 31 and 32.7 nm, respectively using Jade 5.0 upon filtering background. Lattice parameters of

lithiated cathode (a, b, c) are were determined to be (5.789, 9.81, 4.782), respectively with Pnma space group.

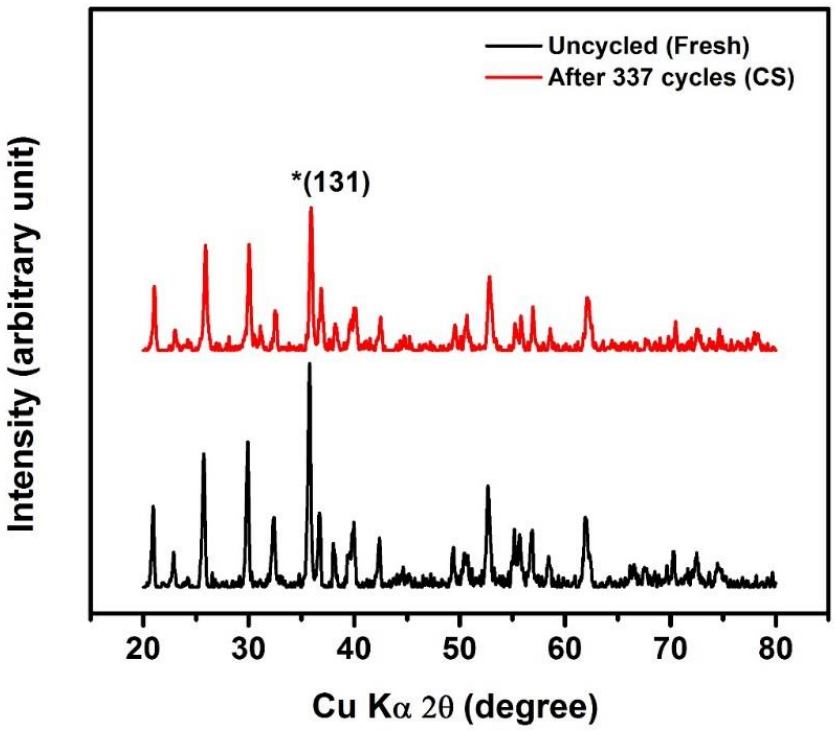

Figure 18. XRD analysis of the cathode material.

8. CAPACITY FADING OF 18650 CELLS UNDER CD MODE

Apart from cycling 26660 LPF cells under charge sustaining mode, similar cycling procedure (see section 6.4) was carried out under charge depleting current (see Figure. 9) on 18650 cells with 2.2 Ah capacity after acquiring new Arbin battery cycler with +/-30 A current range. Cells showed capacity fade of 2 % after 49 cycles at room temperature and 10 % capacity fade after 169 cycles at high temperature. Figure. 19 and Figure. 20 describe

charge/discharge voltage characteristics and cyclablity data of 18650 cells under charge depleting mode.

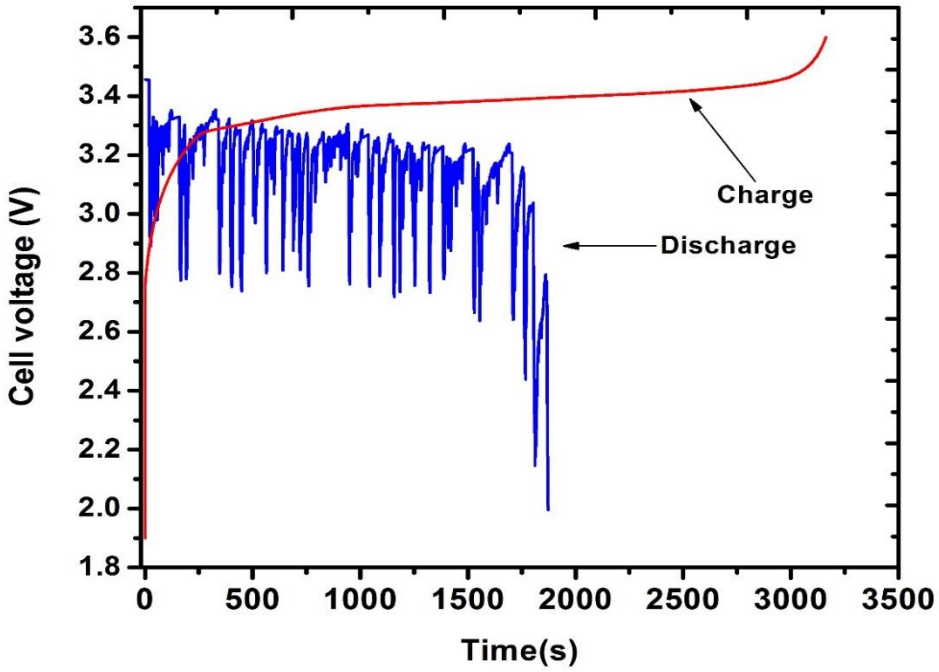

Figure 19. Charge and discharge characteristics of 18650 cells under CD mode.

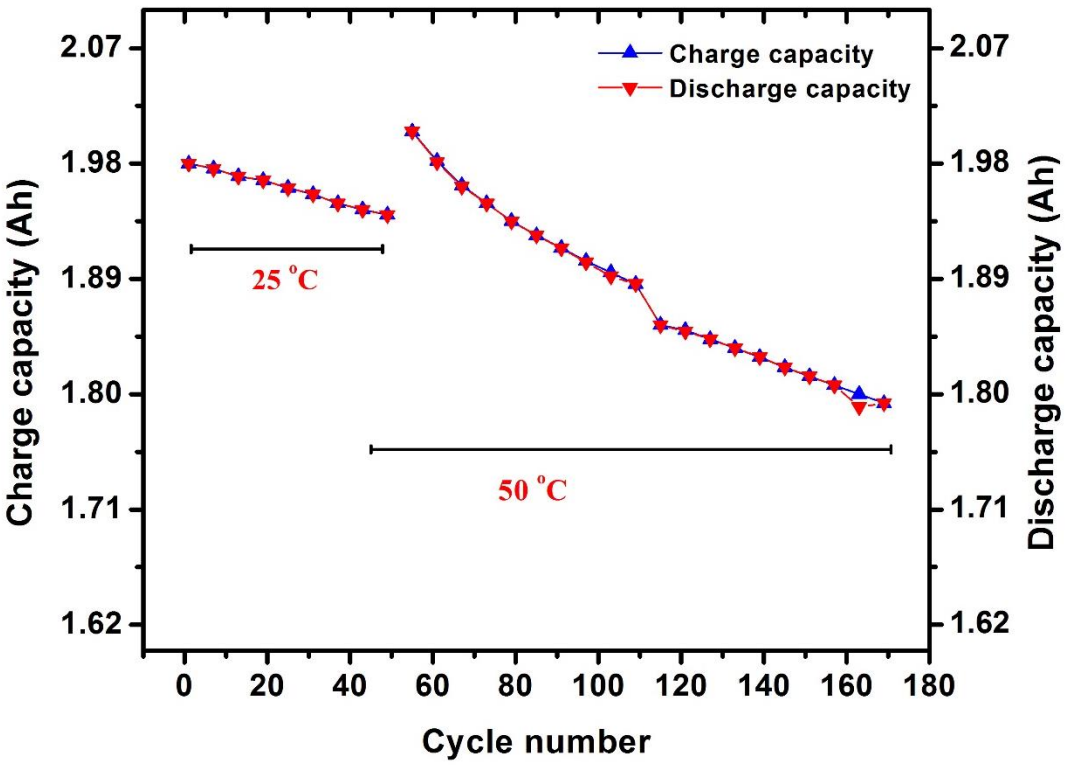

Figure. 20 Cyclabilty data of 18650 cells under charge depleting mode

9. CONCLUSION

Commercial LIBs 26650 (3.6 V, 5 Ah) and 18650 (3.6V, 2.2 Ah) with LFP cathodes were subjected to two different operating modes (CS and CD) based on the FUDS PHEV loads at 50 ^{o}C in order to evaluate the energy and power fading. 18650 cells showed capacity fading of 10 % after 169 cycles at elevated temperature under CD mode and 26650 cells showed only 13 % capacity fading after 337 cycles at elevated temperature under CS mode. Capacity retention rate at elevated temperature was observed to be lower with cycling compared to room temperature. An overall rise in impedance value was observed on cycling and increase in temperature, although impedance values are much lower after the first discharge cycle at elevated temperature compared to room temperature. XRD analysis on CS mode cathode material reveals slight decrease in peak width, signifying an increase in crystallite size with increase in cycle number. Based on the cycling results, 26650 cells (LFP cathode) are viable battery systems for hybrid powertrains under hot and dry weather conditions like Arizona, Texas, and California, due to their better cycle life (~ 13% degradation) at elevated temperatures and relatively lower cost compared to LIBs.

10. FUTURE WORK

Work presented on 18650 cells in the thesis will be continued for life cycle tests, EIS, and XRD analysis. There is a good scope to develop a generic battery ageing model that can predict performance of batteries at different operating conditions and under different drive profiles. TEM study on cathode and anode materials would be essential to study dendrite formation and to observe changes in surface morphology of the electrodes.

11. REFERENCES

[1]. Overview of Greenhouse Gases
http://www3.epa.gov/climatechange/ghgemissions/gases/co2.html, accessed [16.02.24].

[2]. Greenhouse gas emissions from a typical passenger vehicle,
https://www3.epa.gov/otaq/climate/documents/420f14040a.pdf; EPA-420-F-14-040a (2014).

[3]. Markel, Tony, Harshad S. Tataria, and David Howell. *Battery Requirements for Plug in Hybrid Electric Vehicles--analysis and Rationale*. National Renewable Energy Laboratory, 2009.

[4].Chu, Steven, and Arun Majumdar. "Opportunities and challenges for a sustainable energy future." *nature* 488, no. 7411 (2012): 294-303.

[5]Pesaran, Ahmad. *Battery Requirements for Plug-In Hybrid Electric Vehicles: Analysis and Rationale (Presentation)*. No. NREL/PR-540-42469. National Renewable Energy Laboratory (NREL), Golden, CO, 2007.

[6].Zaghib, K., K. Striebel, A. Guerfi, J. Shim, M. Armand, and M. Gauthier. "$LiFePO_4$/polymer/natural graphite: low cost Li-ion batteries." *Electrochimica acta* 50, no. 2 (2004): 263-270.

[7]. Kannan, A. M., Lew Rabenberg, and A. Manthiram. "High capacity surface-modified $LiCoO_2$ cathodes for lithium-ion batteries." *Electrochemical and solid-state letters* 6, no. 1 (2003): A16-A18.

[8].Ehsani, Mehrdad, Yimin Gao, and John M. Miller. "Hybrid electric vehicles: architecture and motor drives." *Proceedings of the IEEE* 95, no. 4 (2007): 719-728.

[9].Emadi, Ali, Kaushik Rajashekara, Sheldon S. Williamson, and Srdjan M. Lukic. "Topological overview of hybrid electric and fuel cell vehicular power system architectures and configurations." *IEEE Transactions on Vehicular Technology* 54, no. 3 (2005): 763-770.

[10].Kim, Namdoo, Ayman Moawad, Neeraj Shidore, and Aymeric Rousseau. "Fuel Consumption and Cost Potential of Different Plug-In Hybrid Vehicle Architectures." *SAE International Journal of Alternative Powertrains* 4, no. 2015-01-1160 (2015): 88-99.

[11].Bianchi, Domenico, Luciano Rolando, Lorenzo Serrao, Simona Onori, Giorgio Rizzoni, Nazar Al-Khayat, Tung-Ming Hsieh, and Pengju Kang. "A rule-based strategy for a series/parallel hybrid electric vehicle: an approach based on dynamic programming." In *ASME 2010 Dynamic Systems and Control Conference*, pp. 507-514. American Society of Mechanical Engineers, 2010.

[12].http://www.greenhoustontx.gov/ev/pdf/evdeploymentguidelines.pdf (accessed on April 1, 2016).

[13].Lukic, Srdjan M., Jian Cao, Ramesh C. Bansal, Fernando Rodriguez, and Ali Emadi. "Energy storage systems for automotive applications." *IEEE Transactions on industrial electronics* 55, no. 6 (2008): 2258-2267.

[14].Budde-Meiwes, Heide, Julia Drillkens, Benedikt Lunz, Jens Muennix, Susanne Rothgang, Julia Kowal, and Dirk Uwe Sauer. "A review of current automotive battery technology and future prospects." *Proceedings of the Institution of Mechanical Engineers, Part D: Journal of Automobile Engineering* 227, no. 5 (2013): 761-776.

[15].Linden, David. "Handbook of batteries." In *Fuel and Energy Abstracts*, vol. 4, no. 36, p. 265. 1995.

[16].Etacheri, Vinodkumar, Rotem Marom, Ran Elazari, Gregory Salitra, and Doron Aurbach. "Challenges in the development of advanced Li-ion batteries: a review." *Energy & Environmental Science* 4, no. 9 (2011): 3243-3262.

[17]. Ehrlich, Grant M. "Lithium-ion batteries." *Handbook of batteries* (2002): 35-53.

[18] Pohjalainen, Elina. "Negative Electrode Materials for Lithium Ion Batteries." (2016).

[19].Goriparti, Subrahmanyam, Ermanno Miele, Francesco De Angelis, Enzo Di Fabrizio, Remo Proietti Zaccaria, and Claudio Capiglia. "Review on recent progress of nanostructured anode materials for Li-ion batteries." *Journal of Power Sources* 257 (2014): 421-443.

[20].Padhi, A. K., K. S. Nanjundaswamy, and J. B. D. Goodenough. "Phospho-olivines as positive-electrode materials for rechargeable lithium batteries. "*Journal of the electrochemical society* 144, no. 4 (1997): 1188-1194.

[21].Andersson, Anna S., Beata Kalska, Lennart Häggström, and John O. Thomas. "Lithium extraction/insertion in LiFePO 4: an X-ray diffraction and Mössbauer spectroscopy study." *Solid State Ionics* 130, no. 1 (2000): 41-52.

[22].Amine, K., J. Liu, and I. Belharouak. "High-temperature storage and cycling of C-LiFePO 4/graphite Li-ion cells." *Electrochemistry Communications* 7, no. 7 (2005): 669-673.

[23]Han, Xuebing, Minggao Ouyang, Languang Lu, Jianqiu Li, Yuejiu Zheng, and Zhe Li. "A comparative study of commercial lithium ion battery cycle life in electrical vehicle: Aging mechanism identification." *Journal of Power Sources*251 (2014): 38-54.

[24].Ramadass, P., Bala Haran, Ralph White, and Branko N. Popov. "Capacity fade of Sony 18650 cells cycled at elevated temperatures: Part I. Cycling performance." *Journal of power sources* 112, no. 2 (2002): 606-613.

[25]Ramadass, P., Bala Haran, Ralph White, and Branko N. Popov "Capacity fade of Sony 18650 cells cycled at elevated temperatures: Part II. Capacity fading analysis", *Journal of power sources* 112, no 2 (2002): 614-620.

[26].Zhang, Yancheng, Chao-Yang Wang, and Xidong Tang. "Cycling degradation of an automotive LiFePO 4 lithium-ion battery." *Journal of Power Sources*196, no. 3 (2011): 1513-1520.

[27].Capasso, Clemente, and Ottorino Veneri. "Experimental analysis on the performance of lithium based batteries for road full electric and hybrid vehicles." *Applied Energy* 136 (2014): 921-930.

[28].Panchal, S., I. Dincer, M. Agelin-Chaab, R. Fraser, and M. Fowler. "Experimental temperature distributions in a prismatic lithium-ion battery at varying conditions." *International Communications in Heat and Mass Transfer*71 (2016): 35-43.

[29]http://www.electricvehiclewiki.com/Battery_Capacity_Loss.(accessed on June 19, 2016)

[30].Tarascon, J-M., and Michel Armand. "Issues and challenges facing rechargeable lithium batteries." *Nature* 414, no. 6861 (2001): 359-367.

[31]https://www.epa.gov/emission-standards-reference-guide/epa-urban-dynamometer-driving-schedule-udds (accessed on June 9, 2016).

[32].Pisu, Pierluigi, and Giorgio Rizzoni. "A comparative study of supervisory control strategies for hybrid electric vehicles." *Control Systems Technology, IEEE Transactions on* 15, no. 3 (2007): 506-518.

[33].Paganelli, Gino, Gabriele Ercole, Avra Brahma, Yann Guezennec, and Giorgio Rizzoni. "General supervisory control policy for the energy optimization of charge-sustaining hybrid electric vehicles." *JSAE review* 22, no. 4 (2001): 511-518.

[34].Paganelli, Gino, Makoto Tateno, Avra Brahma, Giorgio Rizzoni, and Yann Guezennec. "Control development for a hybrid-electric sport-utility vehicle: strategy, implementation and field test results." In *American Control Conference, 2001. Proceedings of the 2001*, vol. 6, pp. 5064-5069. IEEE, 2001.

[35].Kumar, Sushil, Matthew West, Joshua Conter, Megan Cawley, Rashad Maady, and Abdel Mayyas. "Vehicle Plant Model and Supervisory Control Development for a Parallel Pre-Trans Plug-In Hybrid Electric Vehicle." *IFAC-PapersOnLine* 48, no. 15 (2015): 139-146.

[36].Kumar, Sushil. "Fuzzy Logic Based Driving Pattern Recognition for Hybrid Electric Vehicle Energy Management." ARIZONA STATE UNIVERSITY, 2015.

[37]. Peterson, Scott B., Jay Apt, and J. F. Whitacre. "Lithium-ion battery cell degradation resulting from realistic vehicle and vehicle-to-grid utilization."*Journal of Power Sources* 195, no. 8 (2010): 2385-2392.

[38].Huang, Jun, Hao Ge, Zhe Li, and Jianbo Zhang. "Dynamic electrochemical impedance spectroscopy of a three-electrode lithium-ion battery during pulse charge and discharge." *Electrochimica Acta* 176 (2015): 311-320.

[39]. Myung, Seung-Taek, Yashiro Hitoshi, and Yang-Kook Sun. "Electrochemical behavior and passivation of current collectors in lithium-ion batteries." *Journal of Materials Chemistry* 21, no. 27 (2011): 9891-9911.

[40].Andre, D., M. Meiler, K. Steiner, Ch Wimmer, T. Soczka-Guth, and D. U. Sauer. "Characterization of high-power lithium-ion batteries by electrochemical impedance spectroscopy. I. Experimental investigation." *Journal of Power Sources* 196, no. 12 (2011): 5334-5341.

APPENDIX A

SCHEDULE FILE FOR BATTERY CYCLING

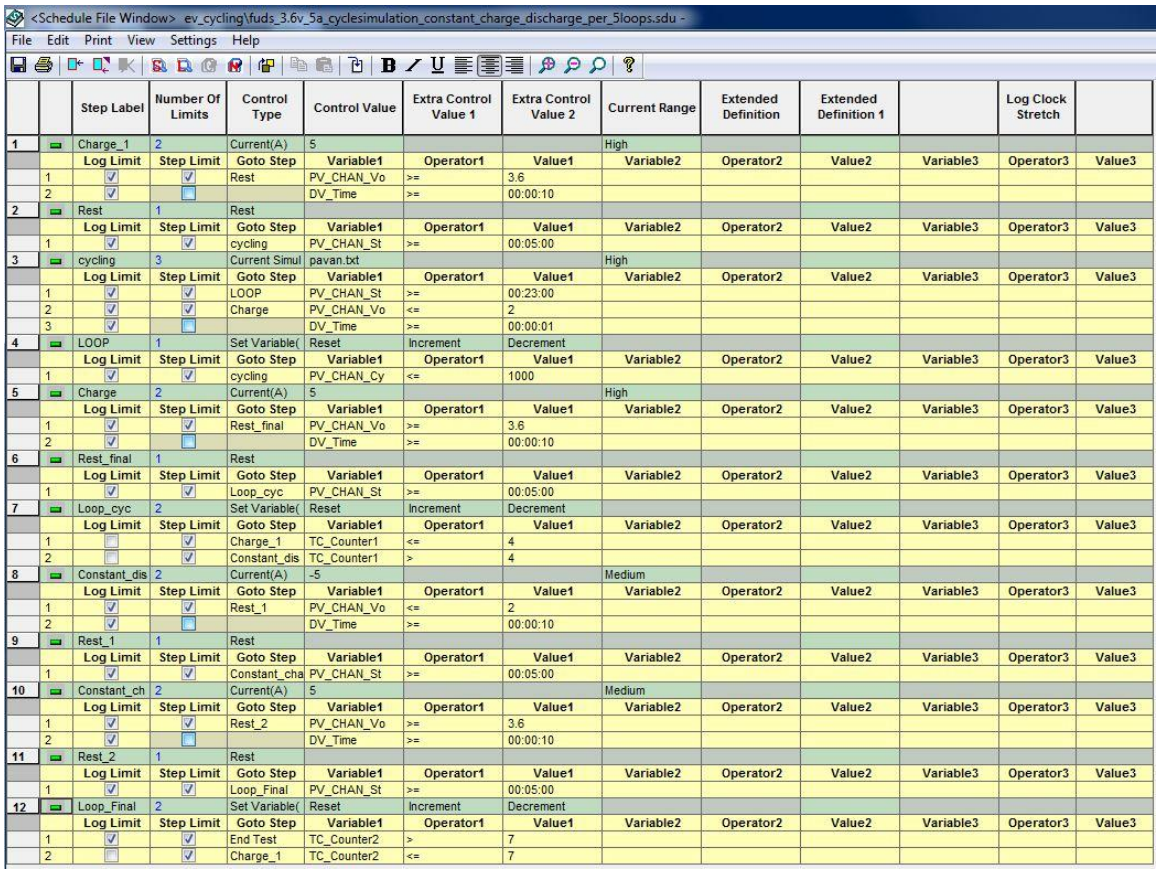

<Schedule File Window> ev_cycling\fuds_3.6v_5a_cyclesimulation_constant_charge_discharge_per_5loops.sdu -

File Edit Print View Settings Help

		Step Label	Number Of Limits	Control Type	Control Value	Extra Control Value 1	Extra Control Value 2	Current Range	Extended Definition	Extended Definition 1		Log Clock Stretch	
1		Charge_1	2	Current(A)	5			High					
		Log Limit	Step Limit	Goto Step	Variable1	Operator1	Value1	Variable2	Operator2	Value2	Variable3	Operator3	Value3
	1	☑	☑	Rest	PV_CHAN_Vo	>=	3.6						
	2	☑	☐		DV_Time	>=	00:00:10						
2		Rest	1	Rest									
		Log Limit	Step Limit	Goto Step	Variable1	Operator1	Value1	Variable2	Operator2	Value2	Variable3	Operator3	Value3
	1	☑	☑	cycling	PV_CHAN_St	>=	00:05:00						
3		cycling	3	Current Simul	pavan.txt			High					
		Log Limit	Step Limit	Goto Step	Variable1	Operator1	Value1	Variable2	Operator2	Value2	Variable3	Operator3	Value3
	1	☑	☑	LOOP	PV_CHAN_St	>=	00:23:00						
	2	☑	☑	Charge	PV_CHAN_Vo	<=	2						
	3	☑	☐		DV_Time	>=	00:00:01						
4		LOOP	1	Set Variable(	Reset	Increment	Decrement						
		Log Limit	Step Limit	Goto Step	Variable1	Operator1	Value1	Variable2	Operator2	Value2	Variable3	Operator3	Value3
	1	☑	☑	cycling	PV_CHAN_Cy	<=	1000						
5		Charge	2	Current(A)	5			High					
		Log Limit	Step Limit	Goto Step	Variable1	Operator1	Value1	Variable2	Operator2	Value2	Variable3	Operator3	Value3
	1	☑	☑	Rest_final	PV_CHAN_Vo	>=	3.6						
	2	☑	☐		DV_Time	>=	00:00:10						
6		Rest_final	1	Rest									
		Log Limit	Step Limit	Goto Step	Variable1	Operator1	Value1	Variable2	Operator2	Value2	Variable3	Operator3	Value3
	1	☑	☑	Loop_cyc	PV_CHAN_St	>=	00:05:00						
7		Loop_cyc	2	Set Variable(	Reset	Increment	Decrement						
		Log Limit	Step Limit	Goto Step	Variable1	Operator1	Value1	Variable2	Operator2	Value2	Variable3	Operator3	Value3
	1	☐	☑	Charge_1	TC_Counter1	<=	4						
	2	☐	☑	Constant_dis	TC_Counter1	>	4						
8		Constant_dis	2	Current(A)	-5			Medium					
		Log Limit	Step Limit	Goto Step	Variable1	Operator1	Value1	Variable2	Operator2	Value2	Variable3	Operator3	Value3
	1	☑	☑	Rest_1	PV_CHAN_Vo	<=	2						
	2	☑	☐		DV_Time	>=	00:00:10						
9		Rest_1	1	Rest									
		Log Limit	Step Limit	Goto Step	Variable1	Operator1	Value1	Variable2	Operator2	Value2	Variable3	Operator3	Value3
	1	☑	☑	Constant_cha	PV_CHAN_St	>=	00:05:00						
10		Constant_ch	2	Current(A)	5			Medium					
		Log Limit	Step Limit	Goto Step	Variable1	Operator1	Value1	Variable2	Operator2	Value2	Variable3	Operator3	Value3
	1	☑	☑	Rest_2	PV_CHAN_Vo	>=	3.6						
	2	☑	☐		DV_Time	>=	00:00:10						
11		Rest_2	1	Rest									
		Log Limit	Step Limit	Goto Step	Variable1	Operator1	Value1	Variable2	Operator2	Value2	Variable3	Operator3	Value3
	1	☑	☑	Loop_Final	PV_CHAN_St	>=	00:05:00						
12		Loop_Final	2	Set Variable(	Reset	Increment	Decrement						
		Log Limit	Step Limit	Goto Step	Variable1	Operator1	Value1	Variable2	Operator2	Value2	Variable3	Operator3	Value3
	1	☑	☑	End Test	TC_Counter2	>	7						
	2	☐	☑	Charge_1	TC_Counter2	<=	7						

APPENDIX B

TORQUE FOR CHARGE SUSTANING MODE FROM S. KUMAR MODEL

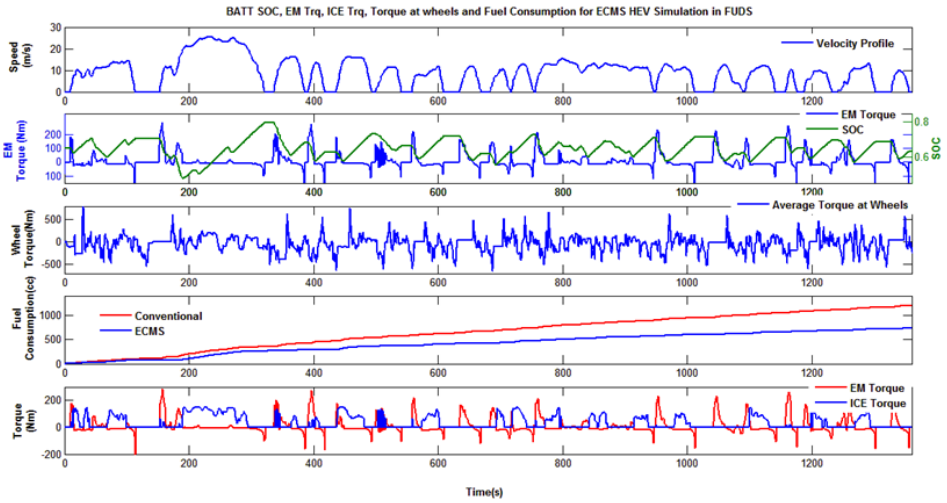
BATT SOC, EM Trq, ICE Trq, Torque at wheels and Fuel Consumption for ECMS HEV Simulation in FUDS
Speed (m/s)
Velocity Profile
EM Torque (Nm)
EM Torque
SOC
SOC
Wheel Torque(Nm)
Average Torque at Wheels
Fuel Consumption(cc)
Conventional
ECMS
Torque (Nm)
EM Torque
ICE Torque
Time(s)